GEOPHYSICS

# Nanosecond structural evolution in shocked coesite

**Xiaokang Feng[1,2]†, Shuning Pan[3]†, Kento Katagiri[4,5], Jiuyang Shi[3], Jia Qu[1,2], Keita Nonaka[4], Cong Liu[6], Liang Sun[7], Pinwen Zhu[2], Norimasa Ozaki[4,5], Takayoshi Sano[5], Yuichi Inubushi[8,9], Kohei Miyanishi[9], Keiichi Sueda[9], Tadashi Togashi[8,9], Makina Yabashi[8,9], Toshinori Yabuuchi[8,9], Hirotaka Nakamura[4], Yoichiro Hironaka[5], Yuhei Umeda[4,10], Yusuke Seto[11], Takuo Okuchi[10], Jian Sun[3]*, Toshimori Sekine[1,4,12]*, Wenge Yang[1]***



**The phase transitions in minerals under shock are crucial for understanding meteorite impact history. Recent time-resolved x-ray diffraction (XRD) studies on silica shocked to 65 GPa proposed the formation of different high-pressure phases between fused silica and quartz. Furthermore, the dynamics of silica behavior under higher pressure need to be investigated, particularly during nonequilibrium superheating before melting. This study examines the time-dependent response of coesite, using laser-driven shock coupled with fast XRD and molecular dynamics simulations with our recently developed machine learning interatomic potential. Our results reveal a transient dense supercooled liquid crystallizes into a semi-disordered d-NiAs-type silica, followed by transforming into either seifertite or stishovite, depending on the pressure. Instead of thermodynamically stable quartz, a back-transformation to coesite phase is identified after release. The complicated phase evolution pathways in shocked coesite provide deeper insights into the high-pressure silica phases observed in the meteorite bombardments on the early Moon, Mars, and Earth.**

## INTRODUCTION

Silica is one of the most abundant minerals found on Earth, terrestrial planets, and rocky meteorites. Understanding silica's high-pressure phase transitions under shock loading is crucial to explore how the early planets formed under impacts, meteorites' history, and the emergence of habitable conditions (*1*–*6*). Recent short-pulsed x-ray diffraction (XRD) studies on shocked fused silica and quartz have clarified their structures in the mixed-phase regions (<65 GPa), highlighted different dynamic behavior of fused silica and quartz, and challenged the long-standing assumption of a uniform phase transition path between the static and shock compression processes (*7*–*9*). These studies emphasize the notable role of the initial silica structures on their shock behavior.

Coesite is a denser high-pressure silica phase (33% denser than fused silica, 20% denser than quartz) with the same tetrahedral coordination as fused silica and quartz. Therefore, it is naturally the next key research target to reveal the dynamic mechanisms of silica polymorphs. Under static compression, $SiO_2$ undergoes a series of thermodynamically-stable phase transitions, including coesite (*C*2/*c* at ~3 GPa), stishovite (rutile type structure, $P4_2/mmm$ at ~10 GPa), a $CaCl_2$ type structure (*Pnnm*, at ~50 GPa), and then seifertite (α-$PbO_2$ type structure, *Pbcn* at ~105 GPa) (*1*, *10*–*14*). It is assumed that under shock loading, coesite will transform into a mixed-phase (coesite and stishovite) region, as well as a stishovite and $CaCl_2$-type structure before melting (*10*). However, there is no direct evidence to confirm this assumption. Before melting, shocked coesite has an abnormal superheating region (SH, 115 to 148 GPa), similar to those found in shocked fused silica (SH, 69 to 80 GPa) and quartz (SH, 94 to 125 GPa) (*15*–*17*). Shen *et al.* (*18*) suggested a nucleation process from shock-induced amorphous silica to stishovite in fused silica and quartz via molecular dynamics (MD) simulations. However, Tracy *et al.* (*8*) observed the formation of d-NiAs-type structure (niccolite-type) or rosiaite-type silica in the shocked quartz up to 65 GPa, instead of the expected stishovite or $CaCl_2$-type silica.

Coesite and stishovite are abundant in the natural samples of terrestrial impactites or meteorites, and seifertite was recently discovered in heavily shocked lunar and Martian meteorites. However, d-NiAs-type silica has not been identified until now (*2*, *6*, *19*, *20*). These crystalline silica phases are often encapsulated in diaplectic glass or dense amorphous silica, implying a possible shock-induced amorphous process before crystallization. The annealing effect during shock release also highlights the absence of d-NiAs-type silica or any potential post-stishovite, while indicating the formation of coesite, stishovite, and amorphous silica. However, the phase evolution path has not been investigated nor has the possible formation of $CaCl_2$-type silica or seifertite under shock compression.

Studies on the structural evolution of shocked coesite are essential for understanding the behavior of silica polymorphs under shock. Previous shock studies investigated fused silica and quartz up to 65 GPa. In this work, we conducted in situ XRD measurements of coesite under nanosecond-duration laser-driven shock with pressure up to 131 GPa, the superheating region, as previously reported (*17*). By combining MD simulations with our developed machine learning interatomic potential (ML-MD), we gained comprehensive insight into the metastable intermediate phases forming by rapid nucleation

[1]Center for High-Pressure Science and Technology Advanced Research, Beijing 100094, China. [2]Synergetic Extreme Condition High-Pressure Science Center, State Key Laboratory of Superhard Materials, College of Physics, Jilin University, Changchun 130012, China. [3]National Laboratory of Solid-State Microstructures, School of Physics and Collaborative Innovation Center of Advanced Microstructures, Nanjing University, Nanjing 210093, China. [4]Graduate School of Engineering, Osaka University, Osaka 565-0871, Japan. [5]Institute of Laser Engineering, Osaka University, Osaka 565-0871, Japan. [6]Extreme Materials Initiative, Earth and Planets Laboratory, Carnegie Institution for Science, 5241 Broad Branch Road NW, Washington, DC 20015, USA. [7]National Key Laboratory of Plasma Physics, Laser Fusion Research Center, Chinese Academy of Engineering Physics, Mianyang 621900, China. [8]Japan Synchrotron Radiation Research Institute, Hyogo 679-5198, Japan. [9]RIKEN SPring-8 Center, Hyogo 679-5148, Japan. [10]Institute for Integrated Radiation and Nuclear Science, Kyoto University, Osaka 590-0494, Japan. [11]Graduate School of Science, Kobe University, Hyogo 657-0013, Japan. [12]Shanghai Key Laboratory of Material Frontiers Research in Extreme Environments, Shanghai Advanced Research in Physical Sciences, Shanghai 201203, China.
*Corresponding author. Email: yangwg@hpstar.ac.cn (W.Y.); toshimori.sekine@hpstar.ac.cn (T.S.); jiansun@nju.edu.cn (J.S.)
†These authors contributed equally to this work.

on a picosecond timescale under shock loading. Our observations reveal the nanosecond dynamic phase transition pathways in non-equilibrium shock conditions and constrain the thermodynamic mechanism of silica polymorphs. The reconstructive transformation can occur in a kinetically limited time imposed by shock-loading (*21*). These findings contribute to our understanding of $SiO_2$ nature under extreme pressure, casting light on the fate of coesite under planetary impacts, and providing clues to the shock response of silicate minerals and thermo-chemical-dynamical conditions during early planetary geological history.

## RESULTS

### The structure of shocked coesite at the earliest time delay

A typical experimental configuration, operated at the Spring-8 Angstrom Compact Free Electron Laser (SACLA) facility, is shown in Fig. 1A. The synthesis method and characterization of polycrystalline coesite are detailed in Materials and Method and fig. S1, as described in our previous work (*17*). The breakout time from the coesite free surface and total travel time through the ablator and coesite were measured using a velocity interferometer system for any reflector (VISAR; fig. S2 and table S2). Hydrodynamic simulations conducted with Multi1D predicts that the arrival at the ablator/coesite interface is about 2.1 to 3.5 ns, depending on the drive laser intensity or peak pressures' variation (fig. S3). The variation of pressures is shown as a function of both time and position, highlighting that the shockwave decays due to the rarefaction effect. Time-resolved x-ray free-electron lasers (XFELs) probing at different delays ($t_D$) reveals insights into $SiO_2$ structural behavior under different high-pressure conditions. Using the measured shocked coesite densities derived from the lattice constants of the detected crystalline phases (table S1), we estimated the corresponding pressures ($P_{EOS}$) experienced by each phase, using the reported pressure-density Hugoniot of coesite (Materials and Method) (*22*).

Figure 1B shows the two represented two-dimensional (2D) diffraction patterns obtained at $P_{EOS} = 131$ GPa ($t_D = 5$ ns) and 41 GPa ($t_D = 6.5$ ns). The azimuthally integrated diffraction profiles across a series of $P_{EOS}$ (41 to 131 GPa) are compiled in Fig. 1C, with the uncompressed coesite peaks masked-out. At the maximum pressure ($P_{EOS} \approx 131$ GPa), a liquid phase (#974560, shown in the flat panel detector panel of Fig. 1A) was detected at $t_D = 4.5$ ns, while at $t_D = 5$ ns, a crystalline d-NiAs-type silica emerged. Early probing at $t_D = 3.5$ ns

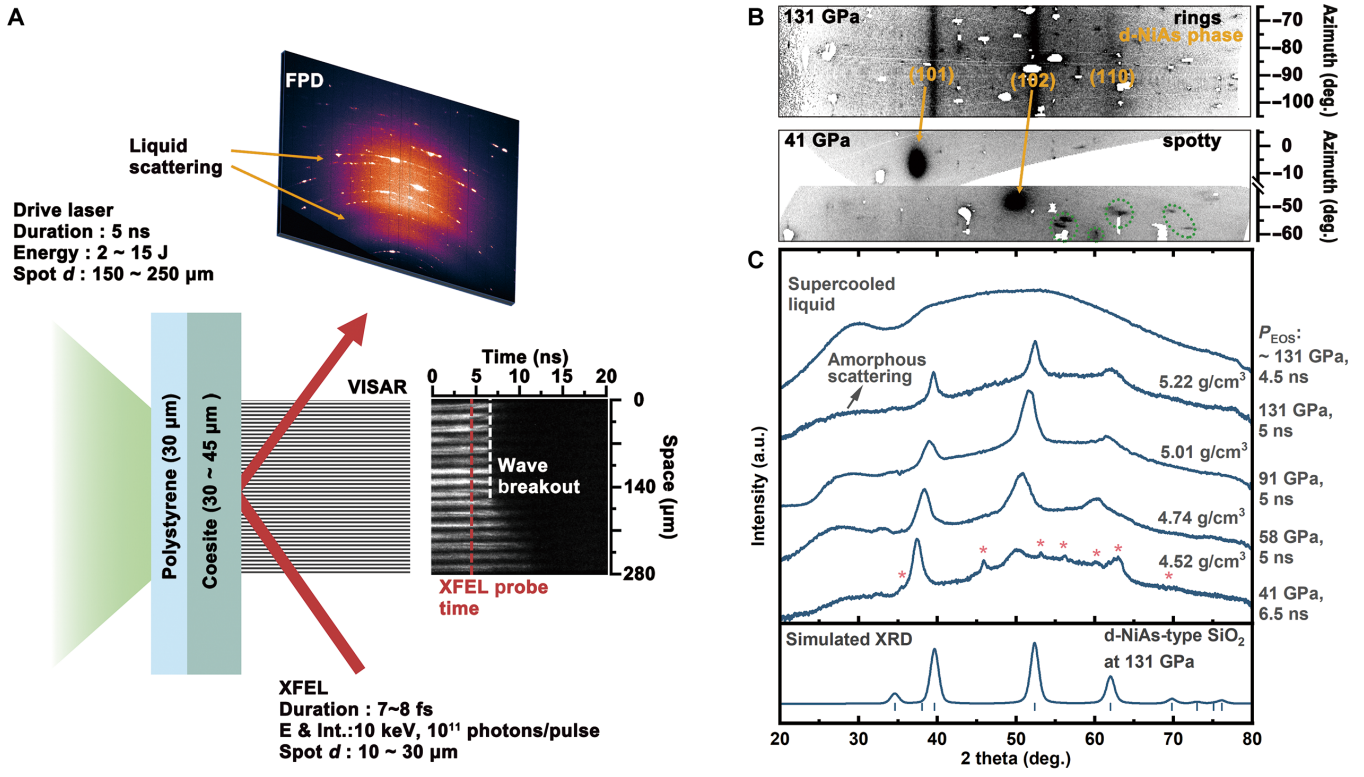


**Fig. 1. Experimental configuration and typical XRD from laser shocked coesite at the earliest time delay.** (**A**) Experimental configuration of the XRD and VISAR measurements at the SACLA BL3 beamline. A typical shock target consists of a polystyrene (30 μm) ablator, and a polycrystalline coesite slab (30 to 45 μm). The shockwave launched by the drive laser goes through the layered target and its breakout timing is recorded by VISAR. The diffraction patterns (example, #974560) are collected by a flat panel detector (FPD). The XFEL probe time delay ($t_D$) was counted from the timing of the drive-laser irradiation ($t_0$, Materials and Method and fig. S2). (**B**) Two representative 2D diffraction patterns were collected at the estimated pressures ($P_{EOS}$) of 131 and 42 GPa, with diffraction peaks from the uncompressed coesite masked out. $P_{EOS}$ are determined by the Hugoniot density-pressure relation (*33*). The continuous diffraction rings seen at 131 GPa and a delay of 5 ns correspond to the (101), (102), and (110) reflections of d-NiAs-type $SiO_2$. These smooth diffraction rings are also observed at 91 and 58 GPa. In contrast, a spotty pattern is observed at 41 GPa with a $t_D = 6.5$ ns. Two separate azimuthally dependent spotty diffraction peaks at 37.4° and 50.0° correspond to the (101) and (102) reflections of d-NiAs-type $SiO_2$, respectively. The peaks marked with the green dashed-circle [pink asterisk symbol in (C)] belong to the unknown silica polymorphs. (**C**) Azimuthally integrated diffraction patterns as a function of compressed pressure. The diffraction spots from the uncompressed coesite portion are masked out for clarity.

(#974549) under the same shock conditions revealed no new phases beyond the initial coesite diffraction, despite the shockwave traveling through coesite for approximately 1.4 ns. This is likely due to the low diffraction efficiency and small amount of liquid present. As the shockwave decayed, the pressure of this liquid phase was estimated to range from 100 to 150 GPa with the hydrodynamic simulation (fig. S3). The positions of the first sharp diffraction peak (FSDP) are plotted as a function of pressure ($P_{EOS}$) in fig. S4B. It shows a trend similar to that of silica glass under equivalent static pressures, though the FSDP shows a lower scattering vector ($Q$) compared to silica glass, due to the thermal effect under shock compression (*8*, *23*–*27*). This indicates consistency in the crystalline and amorphous phases pressures. However, similar of the diffraction patterns make it challenging to distinguish between amorphous solid and liquid. On the basis of the subsequent ultrafast nucleation and ML-MD simulation discussed below, we identified the specific supercooled liquid state at $t_D = 4.5$ ns.

The diffraction patterns measured at $t_D = 5$ ns and 131 GPa show smooth powder rings corresponding to the d-NiAs-type structure and a small amount of residual liquid/amorphous scattering can still be seen from the background profile. Similar diffraction rings of d-NiAs-type silica are observed at 91 and 58 GPa with a 5 ns time delay. There is a higher intensity of amorphous diffraction scattering at 25° to 32° under 91 and 58 GPa compared to 131 GPa, indicating a slower crystallization process under lower pressure and temperature. In contrast, the diffraction pattern at 41 GPa with a time delay of 6.5 ns displays two kinds of azimuthally dependent spotty patterns. The larger spots at about 37.4° and 50.0° are indexed as (101) and (102) reflections of the d-NiAs-type structure, while the (110) peak disappeared. Notably, shocked quartz shows azimuthally dependent diffuse peaks at 25° to 32° (*8*), in contrast to the azimuthally independent amorphous scattering in shocked coesite (Fig. 2). Otzen *et al.* (*28*) suggested that shocked quartz forms a rosiaite-structure silica, which may imply a relatively different transition path between shocked coesite and quartz.

## The experimental phase evolution under the same shock condition

Figure 2 presents the diffraction patterns for shocked coesite at various time delays (4.5 to 10 ns) with a peak $P_{EOS}$ around 131 GPa. The process can be divided into two distinct temporal regions based on the breakout time ($t_1$) of the shockwave, resulting in left-propagated rarefaction waves (fig. S3).

At $t_D = 4.5$ ns, broad diffraction peaks from the supercooled liquid were observed. At 5 ns, polycrystals of the d-NiAs-type $SiO_2$ [$\rho = 5.22(4)$ g/cm$^3$] were detected, demonstrating rapid nucleation and crystallization by 0.5 ns. At $t_D = 6.5$ ns, the spotty diffraction of seifertite [$\rho = 5.32(2)$ g/cm$^3$] appeared, while the d-NiAs-type diffraction rings disappeared. This indicates a phase transition from d-NiAs type to seifertite during continuous recrystallization or grain growth, emphasizing the metastable properties of the d-NiAs-type $SiO_2$.

At $t_D = 8$ ns, seifertite density decreases down to 4.69(5) g/cm$^3$ and partially transforms to stishovite [4.27(2) g/cm$^3$] due to the rarefaction waves launched from the right free surfaces. The textured Debye-Scherrer diffraction pattern (fig. S5) shows seifertite has a strong preferred orientation along the wave propagation direction, while the stishovite pattern shows smooth diffraction rings. Thus, the accompanying grain crushing process arises from rarefaction wave interactions during the seifertite to stishovite transformation.

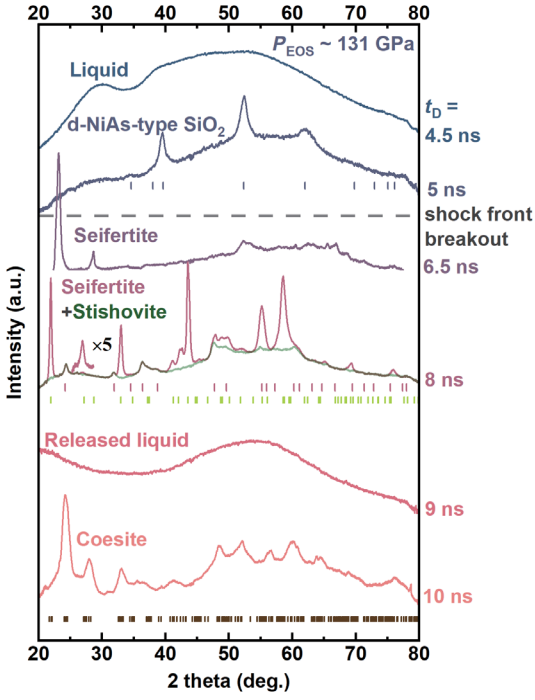


**Fig. 2. The time-resolved structural evolution of shocked coesite at 131 GPa with a time delay ranging between 4.5 and 10 ns.** Integrated diffraction patterns with the initial uncompressed coesite diffraction masked out for clarity. The dashed-gray line indicates the breakout timing of the shock front at the right free surface of coesite. More details about the shockwave travel times in the targets are summarized in table S2. Two representative azimuthally unwrapped XRD patterns with time delays of 5 and 8 ns are presented in Fig. 1B and fig. S5, respectively. The diffractions of the d-NiAs-type structure and stishovite show continuous rings, while the seifertite and released coesite show spotty patterns indicating fast grain growth procedures. The stishovite diffraction signals at 8 ns are marked with a green line.

At $t_D = 9$ ns, the whole sample is in the postreleased state at ambient or even negative pressures. The XRD pattern indicates a partial liquid state because of the high temperature after release. Along the ideal releasing isentropic path, pressure decreases rapidly, while temperature decreases slowly (fig. S6) (*29*, *30*). At 10 ns, coesite, manifesting as spotty diffraction patterns (fig. S7), is formed with a density of 3.43(1) g/cm$^3$. Similar stishovite and coesite formations are observed during or after release when $P_{EOS} = 41$ to 58 GPa, as shown in fig. S8. The same narrow homogenous diffraction patterns of well crystalized coesite were obtained at $t_D = 25$ ns. However, seifertite was only investigated when the peak $P_{EOS}$ reached 131 GPa.

## Simulated structural evolution of the nonequilibrium Hugoniot state

To understand the thermodynamic and structural evolution of shocked coesite, we applied ML-MD simulations using a multiscale shock technique (MSST) (*31*, *32*). The simulated particle velocity and shock velocity Hugoniot points plotted in fig. S9 are consistent with the experimental results (*17*, *33*, *34*). Figure 3 demonstrates the shock response of single-crystal coesite at 125 GPa, along the $z$ axis. A series of simulated XRD patterns under different compression times ($t_{cal.}$) from 20 ps to 1 ns are plotted in comparison with the experimental results (Fig. 3A). By 20 ps of initial compression, a highly disordered phase, supercooled liquid occurs (lower diffusivity, ~$10^{-6}$ cm$^2$/s compared to

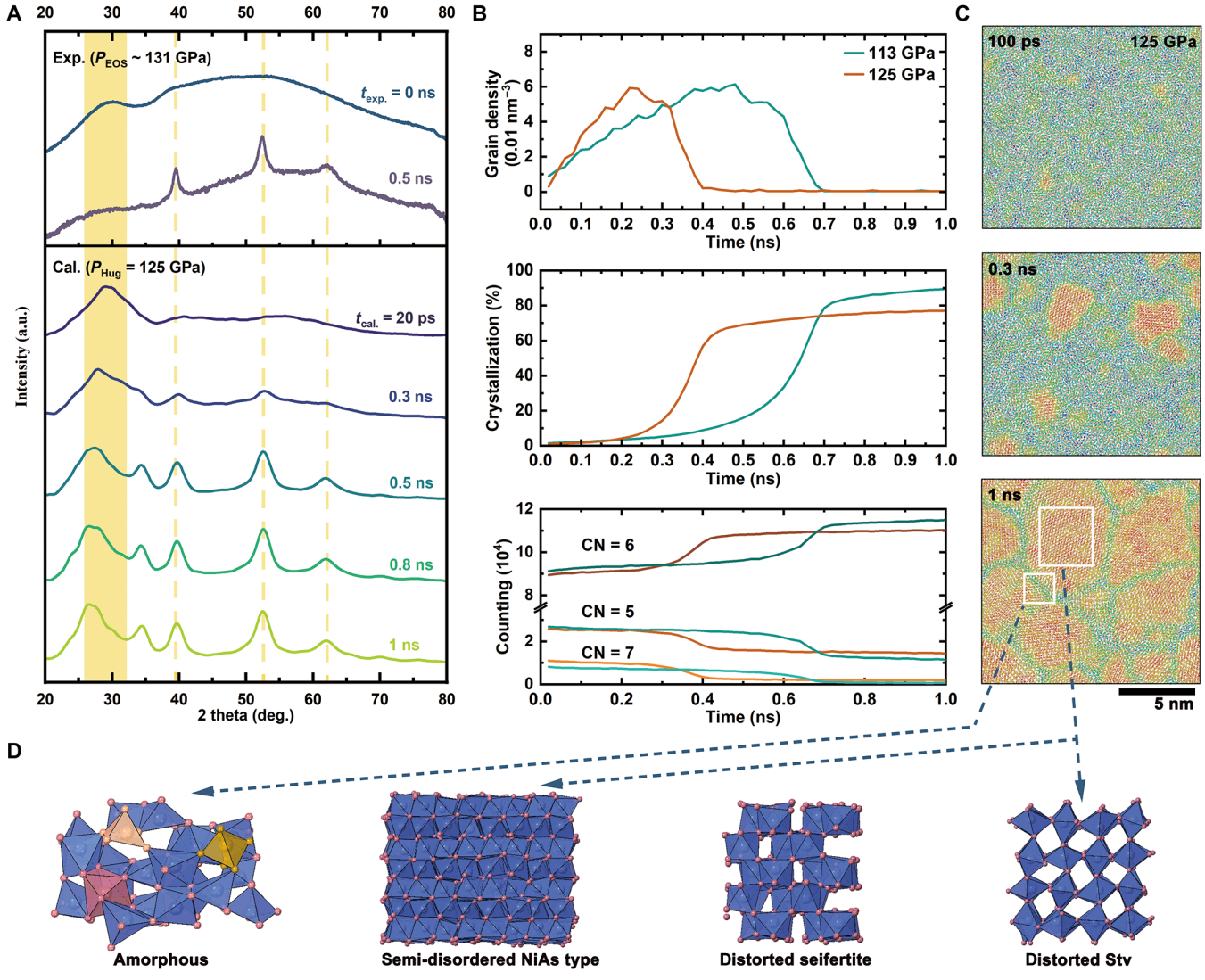


**Fig. 3. MD simulation of the shocked coesite formation.** (**A**) Comparison of XRD patterns between experimental observations at 131 GPa and ML-MD simulations (*z* axis) at 125 GPa. The simulation XRD at 20 ps indicates that the coesite system liquifies (becomes disorder) under shocking, corresponding to the experimental diffraction at the earliest time $t_{cal} = t_{exp.} = 0$ ns ($t_D = 4.5$ ns). Subsequently, new peaks appear afterward and the width narrows for both the simulated and experimental results. (**B**) Time evolution of grain density, crystallization fraction, and coordination number (CN) at pressures of 113 GPa (brown) and 125 GPa (cyan) are compared. The corresponding ultrafast grain merging or recrystallization following the nucleation displays a range of 0.55 to 0.7 ns at 113 GPa and 0.3 to 0.4 ns at 125 GPa. (**C**) Three atomistic views of the shocked coesite (383,999 atoms) for nucleation (100 ps), avalanche growth (0.3 ns), and coalescence (1 ns). The gold and red colors denote Si and O in the crystals respectively, whereas the disordered and boundary atoms are green. (**D**) Representative atomic structures at 1 ns (pink and blue spheres are oxygen and silicon atoms, respectively). At the GB, amorphous $SiO_2$ show complex polymorphs (left): fivefold oxygen (light pink), sixfold oxygen (yellow), and sevenfold oxygen (red). Inside grains, majority of $SiO_2$ show semi-disordered NiAs-type structure (fig. S10), with minority of distorted-seifertite or distorted-stishovite structure (last two panels).

$10^{-5}$ cm$^2$/s of typical liquid). New diffraction peaks appear at 0.3 ns, corresponding to the d-NiAs-type silica. The subsequent, relatively sharp diffraction peaks indicate the crystallization and grain size growth. The grain density and crystallinity over the 1 ns duration at 125 and 113 GPa are summed up in Fig. 3B. At 125 GPa, ultrarapid nucleation occurs in the first $t_{cal} = 0.25$ ns, characterized by the grain density approaching its maximum. The avalanche of grain size growth, with merging nuclei results in grain density decreasing and crystallization increasing, approaching coalescence at about $t_{cal} = 0.4$ ns. By comparison, these processes are slower at 113 GPa, where the rapid nucleation and coalescence of crystallization end at $t_{cal} = 0.45$ and 0.7 ns, respectively. Moreover, it reaches higher crystallinity (about 89%) than that under 125 GPa (about 77%). The changes of coordination numbers (CN) are summarized in the bottom of Fig. 3B. During grain merging, the distribution of sixfold-coordinated (6-CN) Si atom structures rapidly increases, with a reduction in the 7-CN and 5-CN Si atoms. Higher pressures will result in a higher 7-CN and 5-CN content, indicating the presence of a dense amorphous phase.

The representative snapshots of the crystallization process under typical pressure in Fig. 3C illustrate the nucleation, avalanche growth, and coalescence during shock. The initial nucleus size in subnanometer thermally fluctuates. Some of the nuclei merge to grow larger grains, while others dissolve into liquid. During the avalanche growth process, nucleation independently progresses, but

rapid annexation by large nuclei decreases the grain density. Figure 3D shows four representative atomic structures of the coalescence, including a local amorphous arrangement at the grain boundaries (GBs; in green), and a semi-disordered NiAs-type, distorted seifertite, and distorted stishovite in the grains (in gold/red). The leftmost panel shows the $SiO_n$ polyhedral concentrated in the GB, highlighting $SiO_5$, $SiO_6$, and $SiO_7$ polyhedral. Such polyhedral configurations exhibit pronounced distortions from the regular configurations. Inside the crystalline grains, $SiO_6$ octahedra mainly stay in the semi-disordered NiAs-type structure, with selective removal of half of the Si atoms. The face sharing configurations between octahedra are minimized to avoid any strong Coulomb repulsion. In the same hexagonal close-packed stacking layer, the edge-sharing oxygen octahedra form random chains (A layers) but they are mostly corner-linked to the next layer (B layers). On careful inspection, the odd face-sharing octahedra cause substantial local structural distortion. This contradicts the standard disordered-NiAs-type structure, where Si atoms randomly occupy the oxygen octahedra with a 0.5 occupation fraction (*35*). We also found that distorted seifertite and stishovite (or $CaCl_2$ type) structures formed in the grains, which are some of the most stable phases below 125 GPa (*36*). In general, the d-NiAs-type, seifertite, and stishovite (or $CaCl_2$ type) structure share the same superstructure $P6_3/mmc$ (NiAs type). Selective deconstruction of the frameworks of the NiAs-type structure could generate all the above configurations (fig. S11) (*36*, *37*). In summary, we could hypothetically draw the structural evolution path. The d-NiAs-type phase with semi-random silicon distribution nucleates from the shock-induced supercooled liquid phase. Seifertite becomes the stable phase above 100 GPa due to its lower Gibbs free energy compared to stishovite (*36*). Seifertite forms by Si atoms hopping across the neighboring octahedra interfaces of d-NiAs-type $SiO_2$. During decompression, seifertite transforms into stishovite, and subsequently, coesite.

## The shock Hugoniot of coesite

Shocked coesite can experience a superheating state, where the measured temperature is above its melting curves below 150 GPa, as shown in Fig. 4 (*17*). Similar behavior has been observed above the melting curves in fused silica (69 to 80 GPa) and quartz (94 to 125 GPa)

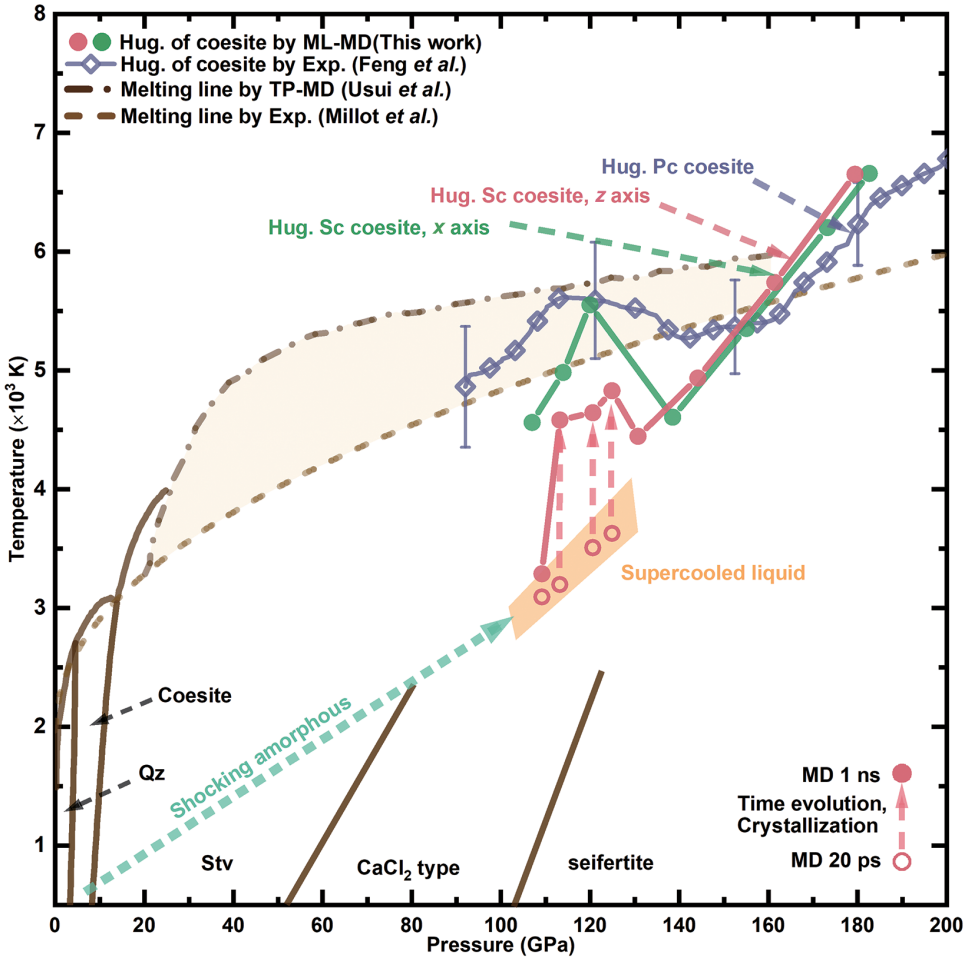


**Fig. 4. Pressure-temperature diagram of shocked coesite.** The P-T relation of shock Hugoniot (cyan arrow) for polycrystalline (Pc) coesite experimentally determined in a previous study, compared with simulated Hugoniots (solid green and red circles) at 1 ns (*17*). A single-crystal (Sc) coesite supercell was used for simulation, with shockwaves along the *x* (green) or *z* (red) direction. Simulated structural evolution crossing between a liquid Hugoniot (open red symbols) and crystallized Hugoniot (solid red symbols) from 20 ps to 1 ns is shown in red dashed arrows. The laser-driven shock data of Pc coesite is shown in purplish gray (open diamond) (*17*). Two melting lines predicted by Simon fitting and two-phase MD (TP-MD) simulation are in the light-brown dashed line (*16*, *48*). The phase boundaries for quartz, coesite, stishovite, $CaCl_2$ type, and seifertite are cited from the literature (*1*, *2*, *49*).

(*16*, *38*). The nucleation and crystallization observed in the present simulations provide detailed insight into such a nonequilibrium and dynamic superheating state. Therefore, we performed further shock simulation of coesite Hugoniot in a range of shock pressures along the *x* and *z* axes of single-crystal coesite, as shown in Fig. 4. The simulated temperature (solid circle) at 125 GPa along the *x* axis is 700 K higher than the *z* axis at 1 ns, highlighting the orientation effect caused by single crystal anisotropy. This also explains the discrepancies between the experimental results of polycrystalline coesite and the simulated results of single crystals. During the crystallization process, as time evolves from $t_{cal}$ = 20 ps (open circle) to $t_{cal}$ = 1 ns (solid circle), the temperature increases due to the entropy and enthalpy difference. When the pressure exceeds 109 GPa, crystallization becomes extremely fast resulting in a sudden rise in temperature within a nanosecond. When shock pressure is higher than 130 GPa, the coesite directly transforms into a typical liquid state. The nucleation and crystallization will not occur, as well as the associated temperature rising. Hence, the solidification temperature at $t_{cal}$ = 1 ns before 130 GPa is higher than the liquid temperature, accounting for the experimental superheating state in shocked coesite (*17*).

## DISCUSSIONS

The time-resolved phase transition paths under various shocking pressure are summarized in Fig. 5. Initially, the d-NiAs-type phase crystallizes first and seifertite appears afterward at pressure above 100 GPa. Stishovite appears third and acts as the key node phase during the pressure release, when the density approaches its value at ambient conditions. Coesite is the final crystalline product after release at $t_D$ = 10 to 25 ns for all samples.

This structural evolution path of shocked coesite is different from shocked fused silica and α-quartz. Under shock compression, fused silica transforms into stishovite, whereas α-quartz transforms to d-NiAs-type or rosiaite-type $SiO_2$ at about 60 GPa (*7*–*9*). The stishovite phase could be quenched from shocked fused silica. However, the shocked quartz is a mixture of amorphous and back-transformed quartz after release. In comparison, under static compression with laser heating, stishovite could be obtained from either α-quartz or fused silica, while d-NiAs type could only be synthesized at lower temperature (<1600 K) with precursor amorphous $SiO_2$. Subsequent heating up to 1800 K produced a stishovite or $CaCl_2$-type structure (*13*). Analogously, it is logical that the supercooled liquid phase initially forms under shock loading on quartz and coesite, followed by the nucleation of d-NiAs-type $SiO_2$. However, because of the lower density of fused silica, higher Hugoniot temperature will be generated in shocked fused silica compared to quartz and coesite at the same pressure, favoring the formation of a stishovite structure instead of the metastable d-NiAs-type $SiO_2$.

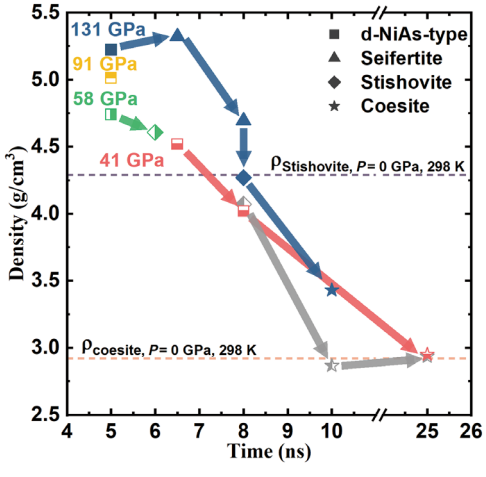


**Fig. 5. Density path of shocked coesite with time.** The density was estimated from the XRD data for the detected phase and time corresponds to the XFEL time delay. Data are listed in table S1. The colors correspond to the shots, and the square, triangle, diamond, and star symbols are phases of the d-NiAs-type phase, seifertite, stishovite, and coesite, respectively.

The back-transformation to coesite is counterintuitive as quartz or fused silica should be the most thermodynamically stable phases under the annealing effect during pressure release, where the pressure decreases rapidly and temperature decreases slowly. It is likely that atomistic neighbor memories are preserved in the limited timescale throughout the entire process. However, our simulations on shocked coesite do not support the preservation of nearest-atomic memories, as almost all tetrahedral configurations of the silicon atoms are destroyed initially within $t_{cal}$ = 20 ps. This memory-like effect in the silica under nanosecond shock loading should be related to the kinetic effect (*8*, *9*). Considering that the diffusivity of supercooled liquid is 10 times less than that of typical liquid, most atoms cannot move through a distance of two atomic bond length before solidification, which presents in the possibility of topotactic structures. However, testing the hypothesis that the submedium range topological order can be preserved in a nanosecond shock process with limited diffusion is extremely challenging. Further advanced experiments with a controlled strain rate are required to reinvestigate the dynamic process in greater detail.

The structural evolution path in this study provides clues for forming the post-stishovite phases. Seifertite has been found in the lunar meteorite, NWA 4734, and Martian meteorite (*5*, *19*), Shergotty, but $CaCl_2$-type silica has not been found yet despite its stability between stishovite and seifertite on the $SiO_2$ phase diagram. The shock features and veins are known to indicate their past heavily shocked condition. The accompanying stishovite in NWA 4734 observed far from the shock vein could be formed at lower temperature than seifertite close to the vein (*19*). Therefore, stishovite is likely a product in the releasing process, rather than directly formed in the shock-compressed state. Consequently, the Clapeyron slope of the boundary between stishovite and seifertite will be positive, which aligns with synthetic experiments (*12*, *19*, *39*). Thus, the maximum shock pressure in NWA 4734 may have reached 100 GPa according to the present study. However, the presence of additional elements in natural seifertite, such as aluminum, sodium, and hydrogen/water, will affect phase boundaries, and introduce variations in estimating the impact pressures (*40*).

## MATERIALS AND METHODS

### Experimental setup

The synthesis detail of bulk transparent coesite is described in our previous article (*17*). Precursor fused silica was completely transformed to coesite using a multistep high-pressure and high-temperature treatment in a cubic press (SPD, 6*14400, State Key Lab of Superhard Materials, Jilin University, Changchun, China). The bulk density ($\rho_0$) is 2.92 g/cm$^3$, measured by the Archimedes

method, and the XRD pattern characterization on the synthesized coesite powder (fig. S1B) was conducted on a Rigaku D/Max-2550 X-ray diffractometer (State Key Laboratory of Inorganic Synthesis and Preparative Chemistry, Jilin University, Changchun, China). The polycrystalline coesite cylinders were initially sectioned into disks with a thickness of 500 μm and polished from both sides to achieve the target thickness (30 to 45 μm). Each target was stuck together with an ablator polystyrene layer of about 30 μm (Fig. 1A).

The experiments were conducted at the SACLA (*41*). The shockwave was launched by a flat-top drive laser (DL, Hamamatsu Photonics K. K., Japan) with a spot diameter 150 to 250 μm and a pulse duration of 5 ns (*41*). Pressures were adjusted by varying the DL energy (<10 TW/cm$^2$). A VISAR system was used to record the breakout timing ($t_1$) from the coesite free surface. However, the free surface velocity could not be measured because the reflectivity intensity dropped during the shockwave breakout. The diffraction patterns were taken using the SACLA XFEL (10 keV, 7 to 8 fs duration, an average of $10^{11}$ photons each pulse, spot diameter H30 × V10 μm$^2$) with different time delays ($t_D$), referring to the irradiation timing of the drive laser ($t_0$) (*41*).

### Calibration of $t_0$ and travel time determination in the samples

Figure S2A illustrates the drive laser pattern irradiated on a Kapton film, as recorded by the streak camera. The probe laser was not used during data collection. The average intensity profile was analyzed, and a Gaussian fit was applied to its derivative. The peak of the Gaussian fit, representing the slope of the intensity profile, indicates the arrival time ($t_0$) of the drive laser. A representative VISAR image for shot #974560 (seen in Fig. 1) and the intensity of the reflected signal are presented in fig. S2B. As detailed above, the free surface velocity could not be determined. Furthermore, the center position of the drive laser was offset to avoid the damaged pixels in the streak camera (*42*).

The breakout timing ($t_1$) was determined by applying Gaussian fitting to the derivative of the signal. The uncertainty was calculated as the SD of the statistical distribution of the peak positions from the Gaussian fits on each fringe. Thus, the whole travel time in the targets (polystyrene, glue, and coesite) was estimated as $t = t_1 - t_0$, as summarized in table S2.

### Pressure determination by the Hugoniot relation based on density

Using densities refined from the XRD patterns and Hugoniot relation reported by Luo *et al.* (*33*), we determined the pressures for each crystalline phase (table S1). This Hugoniot relation provides the equation of state (EOS) for shocked coesite into the stishovite or post-stishovite region. In addition, we assumed that the release pressures of the stishovite or post-stishovite phases follow this Hugoniot relation. Error propagation was estimated by a Monte Carlo calculation with 10,000 runs. Notably, the amorphous phase coexists with the crystalline phases but could not be quantified using this method. Additional pressures evaluation for the amorphous phase, derived from its FSDP, is shown in fig. S4. The relationship between the FSDP positions and the pressures of crystalline phases approximately aligns with those determined under static compression. Although the FSDP positions are at lower *Q* values due to the temperature effect. This suggests that the pressure of the detected amorphous phase is likely below 130 GPa approximately.

### Hydrodynamics simulated by Multi 1D

A series of simulations were conducted using the Multi1D under the applied laser conditions (*43*). The simulations reproduced the breakout time of the shockwave from the coesite sample's back surface. The peak pressures are summarized in table S2. A representative hydrodynamic simulation for shot #975235 is presented in fig. S3. The rarefaction effect results in strong decay of the shockwave, with pronounced variation in pressures or density as a function of both time and position. In an ideal scenario, the shock front generated in the polystyrene layer propagates into coesite at approximately 2.1 ns, resulting in a peak pressure of approximately 200 to 270 GPa (region 1). At around 3.5 ns, the rarefaction wave, reflected from the left surface of the ablator layer, begins to propagate into the post-shocked coesite, placing the material in a quasi-steady high-pressure state (region 2, 100 to 150 GPa). This quasi-steady high-pressure state will decrease to about 10 to 70 GPa (region 3), due to the rarefaction effect arising from the right free surface of the coesite layer. After the drive laser stops, accompanied by additional rarefaction waves, the sample returns to ambient or even negative pressures (*42*). The XFEL probe time delays were aligned with the hydrodynamic simulations. Shot #975235, collected at $t_D = 5$ ns, corresponds to the region 2 (fig. S3). In comparison, shot #975253, conducted at the same drive-laser power, but at $t_D = 8$ ns, corresponds to region 3. Shot #975245, taken at $t_D = 10$ ns, captures the sample in the ambient or negative pressure region.

### Shock velocity analysis based on the travel time

Assuming that the re-shocked polystyrene follows its reflected Hugoniot relation, the average shock velocity ($U_{s,cst}$) in coesite can be estimated using equations, given the thicknesses of polystyrene ($x_{CH}$) and coesite ($x_{cst}$), along with the total travel time ($t$) in the targets (*42*):

$$t = \frac{x_{CH}}{U_{s,CH}} + \frac{x_{cst}}{U_{s,cst}} \quad (1)$$

$$P_{CH} = \rho_{0,\ CH}\left(2U_{p,CH} - U_{p,cst}\right)\left[a_{CH} + b_{CH}\left(2U_{p,CH} - U_{p,cst}\right)\right] \quad (2)$$

$$P_{cst} = \rho_{0,\ cst}U_{p,cst}\left(a_{cst} + b_{cst}U_{p,cst}\right) \quad (3)$$

$$P_{interface} = P_{CH} = P_{cst} \quad (4)$$

where $\rho_{0,i}$, $U_{p,i}$, and $U_{s,i}$ ($i$ = CH, cst) represents the initial density, particle velocity, and shock velocity for polystyrene and coesite, respectively (*44*). The coefficients $a_i$ and $b_i$ are defined by the Hugoniot relation $U_{s,i} = a_i + b_iU_{p,i}$. The results are summarized in the table S3, while error propagation was estimated by a Monte Carlo calculation with 10,000 runs.

### MD simulations

Our MD simulations use the MSST within the GPUMD package (*31*, *32*). Adhering to the Euler equations for compression flow, MSST uses a specialized Lagrangian, facilitating the convergence of the simulation cell to the Hugoniot relation $E - E_0 = \frac{1}{2}(p + p_0)(v_0 - v)$ in a brief time. Because of its focus on a limited region behind the

shock front, MSST substantially reduces computational costs and has been applied across various systems (*18*, *45*). Our simulation cells consist of around 400,000 atoms.

To achieve an optimal balance between the accuracy and computational cost for large systems, we used neuroevolutionary machine learning potentials (*46*). The training data are based on a recently published paper (*47*). The configurations in the training data were carefully generated and calculated with a highly precise density functional theory calculation. It contains the crystal structure of α-quartz, coesite, stishovite, etc. We used additional configurations to the training set to improve its performance under high pressure. We performed ab initio MD simulation of seifertite and selected the configurations from the trajectories to add to the training set. Since the Si atoms in the NiAs-type structure are randomly distributed among possible sites, we generated disordered NiAs-type structures and added them to the training set. The overall training error is shown in fig. S15.

## Supplementary Materials

**This PDF file includes:**

Figs. S1 to S15
Tables S1 to S3
References

## REFERENCES AND NOTES


1. T. Duffy, N. Madhusudhan, K. K. M. Lee, "Mineralogy of super-earth planets" in *Treatise on Geophysics (Second Edition),* G. Schubert, Ed. (Elsevier, Oxford, 2015), pp. 149–178.
2. M. Kayama, H. Nagaoka, T. Niihara, Lunar and martian silica. *Minerals* **8**, 267 (2018).
3. W. Wang, Y. Xu, D. Sun, S. Ni, R. Wentzcovitch, Z. Wu, Velocity and density characteristics of subducted oceanic crust and the origin of lower-mantle heterogeneities. *Nat. Commun.* **11**, 64 (2020).
4. C. Liu, J. Shi, H. Gao, J. Wang, Y. Han, X. Lu, H.-T. Wang, D. Xing, J. Sun, Mixed coordination silica at megabar pressure. *Phys. Rev. Lett.* **126**, 035701 (2021).
5. T. G. Sharp, A. E. Goresy, B. Wopenka, M. Chen, A post-stishovite $SiO_2$ polymorph in the meteorite Shergotty: Implications for impact events. *Science* **284**, 1511–1513 (1999).
6. E. Ohtani, S. Ozawa, M. Miyahara, Y. Ito, T. Mikouchi, M. Kimura, T. Arai, K. Sato, K. Hiraga, Coesite and stishovite in a shocked lunar meteorite, Asuka-881757, and impact events in lunar surface. *Proc. Natl. Acad. Sci. U.S.A.* **108**, 463–466 (2011).
7. A. E. Gleason, C. A. Bolme, H. J. Lee, B. Nagler, E. Galtier, R. G. Kraus, R. Sandberg, W. Yang, F. Langenhorst, W. L. Mao, Time-resolved diffraction of shock-released $SiO_2$ and diaplectic glass formation. *Nat. Commun.* **8**, 1481 (2017).
8. S. J. Tracy, J. Turneaure Stefan, S. Duffy Thomas, Structural response of alpha-quartz under plate-impact shock compression. *Sci. Adv.* **6**, eabb3913 (2020).
9. S. J. Tracy, S. J. Turneaure, T. S. Duffy, In situ x-ray diffraction of shock-compressed fused silica. *Phys. Rev. Lett.* **120**, 135702 (2018).
10. J. A. Akins, T. J. Ahrens, Dynamic compression of $SiO_2$: A new interpretation. *Geophys. Res. Lett.* **29**, 1394 (2002).
11. O. Tschauner, S.-N. Luo, P. D. Asimow, T. J. Ahrens, Recovery of stishovite-structure at ambient conditions out of shock-generated amorphous silica. *Am. Mineral.* **91**, 1857–1862 (2006).
12. M. Murakami, K. Hirose, S. Ono, Y. Ohishi, Stability of $CaCl_2$-type and α-$PbO_2$-type $SiO_2$ at high pressure and temperature determined by in-situ x-ray measurements. *Geophys. Res. Lett.* **30**, 1207 (2003).
13. V. P. Prakapenka, G. Shen, L. S. Dubrovinsky, M. L. Rivers, S. R. Sutton, High pressure induced phase transformation of $SiO_2$ and $GeO_2$: Difference and similarity. *J. Phys. Chem. Solid* **65**, 1537–1545 (2004).
14. L. S. Dubrovinsky, S. K. Saxena, P. Lazor, R. Ahuja, O. Eriksson, J. M. Wills, B. Johansson, Experimental and theoretical identification of a new high-pressure phase of silica. *Nature* **388**, 362–365 (1997).
15. D. G. Hicks, T. R. Boehly, P. M. Celliers, J. H. Eggert, E. Vianello, D. D. Meyerhofer, G. W. Collins, Shock compression of quartz in the high-pressure fluid regime. *Phys. Plasmas* **12**, 082702 (2005).
16. M. Millot, N. Dubrovinskaia, A. Černok, S. Blaha, L. Dubrovinsky, D. G. Braun, P. M. Celliers, G. W. Collins, J. H. Eggert, R. Jeanloz, Shock compression of stishovite and melting of silica at planetary interior conditions. *Science* **347**, 418–420 (2015).
17. X. Feng, K. Katagiri, J. Qu, K. Nonaka, L. Sun, P. Zhu, N. Ozaki, T. Sano, T. Sekine, W. Yang, Shock compression of coesite up to 950 GPa. *Geophys. Res. Lett.* **51**, e2024GL109873 (2024).
18. Y. Shen, S. B. Jester, T. Qi, E. J. Reed, Nanosecond homogeneous nucleation and crystal growth in shock-compressed $SiO_2$. *Nat. Mater.* **15**, 60–65 (2016).
19. M. Miyahara, S. Kaneko, E. Ohtani, T. Sakai, T. Nagase, M. Kayama, H. Nishido, N. Hirao, Discovery of seifertite in a shocked lunar meteorite. *Nat. Commun.* **4**, 1737 (2013).
20. A. E. Goresy, L. Dubrovinsky, T. G. Sharp, S. K. Saxena, M. Chen, A monoclinic post-stishovite polymorph of silica in the Shergotty meteorite. *Science* **288**, 1632–1634 (2000).
21. F. Langenhorst, A. Deutsch, Shock metamorphism of minerals. *Elements* **8**, 31–36 (2012).
22. S. N. Luo, J. L. Mosenfelder, P. D. Asimow, T. J. Ahrens, Stishovite and its implications in geophysics: New results from shock-wave experiments and theoretical modeling. *Phys. Usp.* **45**, 435–439 (2002).
23. Y. Kono, Y. Shu, C. Kenney-Benson, Y. Wang, G. Shen, Structural evolution of $SiO_2$ glass with si coordination number greater than 6. *Phys. Rev. Lett.* **125**, 205701 (2020).
24. C. Prescher, V. B. Prakapenka, J. Stefanski, S. Jahn, L. B. Skinner, Y. Wang, Beyond sixfold coordinated Si in $SiO_2$ glass at ultrahigh pressures. *Proc. Natl. Acad. Sci. U.S.A.* **114**, 10041–10046 (2017).
25. T. Sato, N. Funamori, Sixfold-coordinated amorphous polymorph of $SiO_2$ under high pressure. *Phys. Rev. Lett.* **101**, 255502 (2008).
26. T. Sato, N. Funamori, High-pressure structural transformation of $SiO_2$ glass up to 100 GPa. *Phys. Rev. B* **82**, 184102 (2010).
27. Y. Tange, Y. Nishihara, T. Tsuchiya, Unified analyses for P-V-T equation of state of MgO: A solution for pressure-scale problems in high P-T experiments. *J. Geophys. Res. Solid Earth* **114**, B03028 (2009).
28. C. Otzen, H.-P. Liermann, F. Langenhorst, Evidence for a rosiaite-structured high-pressure silica phase and its relation to lamellar amorphization in quartz. *Nat. Commun.* **14**, 606 (2023).
29. M. Misawa, E. Ryuo, K. Yoshida, R. K. Kalia, A. Nakano, N. Nishiyama, F. Shimojo, P. Vashishta, F. Wakai, Picosecond amorphization of $SiO_2$ stishovite under tension. *Sci. Adv.* **3**, e1602339 (2017).
30. S. N. Luo, T. J. Ahrens, P. D. Asimow, Polymorphism, superheating, and amorphization of silica upon shock wave loading and release. *J. Geophys. Res. Solid Earth* **108**, 2421 (2003).
31. Z. Fan, Y. Wang, P. Ying, K. Song, J. Wang, Y. Wang, Z. Zeng, K. Xu, E. Lindgren, J. M. Rahm, A. J. Gabourie, J. Liu, H. Dong, J. Wu, Y. Chen, Z. Zhong, J. Sun, P. Erhart, Y. Su, T. Ala-Nissila, GPUMD: A package for constructing accurate machine-learned potentials and performing highly efficient atomistic simulations. *J. Chem. Phys.* **157**, 114801 (2022).
32. E. J. Reed, L. E. Fried, J. D. Joannopoulos, A method for tractable dynamical studies of single and double shock compression. *Phys. Rev. Lett.* **90**, 235503 (2003).
33. S. N. Luo, J. L. Mosenfelder, P. D. Asimow, T. J. Ahrens, Direct shock wave loading of stishovite to 235 GPa: Implications for perovskite stability relative to an oxide assemblage at lower mantle conditions. *Geophys. Res. Lett.* **29**, 1691 (2002).
34. M. A. Podurets, Polymorphism of silica in shock waves and equation of state of coesite and stishovite. *Izv. Akad. Nauk SSSR Fiz. Zemli* **17**, 9–15 (1981).
35. J. Haines, J. M. Léger, C. Chateau, Transition to a crystalline high-pressure phase in alpha-$GeO_2$ at room temperature. *Phys. Rev. B* **61**, 8701–8706 (2000).
36. D. M. Teter, R. J. Hemley, G. Kresse, J. Hafner, High pressure polymorphism in silica. *Phys. Rev. Lett.* **80**, 2145–2148 (1998).
37. S. Ivantchev, E. Kroumova, J. Perez-Mato, J. Igartua, G. Madariaga, H. Wondratschek, Supergroups - A computer program for the determination of the supergroups of the space groups. *J. Appl. Cryst.* **35**, 511–512 (2002).
38. D. G. Hicks, T. R. Boehly, J. H. Eggert, J. E. Miller, P. M. Celliers, G. W. Collins, Dissociation of liquid silica at high pressures and temperatures. *Phys. Rev. Lett.* **97**, 025502 (2006).
39. N. Sun, W. Shi, Z. Mao, C. Zhou, V. B. Prakapenka, High pressure-temperature study on the thermal equations of state of seifertite and $CaCl_2$-type $SiO_2$. *J. Geophys. Res. Solid Earth* **124**, 12620–12630 (2019).
40. D. L. Lakshtanov, S. V. Sinogeikin, K. D. Litasov, V. B. Prakapenka, H. Hellwig, J. Wang, C. Sanches-Valle, J.-P. Perrillat, B. Chen, M. Somayazulu, J. Li, E. Ohtani, J. D. Bass, The post-stishovite phase transition in hydrous alumina-bearing $SiO_2$ in the lower mantle of the earth. *Proc. Natl. Acad. Sci. U.S.A.* **104**, 13588–13590 (2007).
41. Y. Inubushi, T. Yabuuchi, T. Togashi, K. Sueda, K. Miyanishi, Y. Tange, N. Ozaki, T. T. Matsuoka, R. Kodama, T. Osaka, S. Matsuyama, K. Yamauchi, H. Yumoto, T. Koyama, H. Ohashi, K. Tono, M. Yabashi, Development of an experimental platform for combinative use of an XFEL and a high-power nanosecond laser. *Appl. Sci.* **10**, 2224 (2020).
42. K. Katagiri, N. Ozaki, S. Ohmura, B. Albertazzi, Y. Hironaka, Y. Inubushi, K. Ishida, M. Koenig, K. Miyanishi, H. Nakamura, M. Nishikino, T. Okuchi, T. Sato, Y. Seto, K. Shigemori, K. Sueda, Y. Tange, T. Togashi, Y. Umeda, M. Yabashi, T. Yabuuchi, R. Kodama, Liquid structure of tantalum under internal negative pressure. *Phys. Rev. Lett.* **126**, 175503 (2021).
43. R. Ramis, R. Schmalz, J. Meyer-Ter-Vehn, MULTI - A computer code for one-dimensional multigroup radiation hydrodynamics. *Comput. Phys. Commun.* **49**, 475–505 (1988).
44. M. A. Barrios, D. G. Hicks, T. R. Boehly, D. E. Fratanduono, J. H. Eggert, P. M. Celliers, G. W. Collins, D. D. Meyerhofer, High-precision measurements of the equation of state of hydrocarbons at 1–10 Mbar using laser-driven shock waves. *Phys. Plasmas* **17**, 056307 (2010).

45. N. Goldman, E. J. Reed, L. E. Fried, I. F. William Kuo, A. Maiti, Synthesis of glycine-containing complexes in impacts of comets on early Earth. *Nat. Chem.* **2**, 949–954 (2010).
46. Z. Fan, Z. Zeng, C. Zhang, Y. Wang, K. Song, H. Dong, Y. Chen, T. Ala-Nissila, Neuroevolution machine learning potentials: Combining high accuracy and low cost in atomistic simulations and application to heat transport. *Phys. Rev. B* **104**, 104309 (2021).
47. L. C. Erhard, J. Rohrer, K. Albe, V. L. Deringer, A machine-learned interatomic potential for silica and its relation to empirical models. *npj Comput. Mater.* **8**, 90 (2022).
48. Y. Usui, T. Tsuchiya, Ab initio two-phase molecular dynamics on the melting curve of $SiO_2$. *J. Earth Sci.* **21**, 801–810 (2010).
49. R. Fischer, A. Campbell, B. Chidester, D. Reaman, E. C. Thompson, J. Pigott, V. Prakapenka, J. Smith, Equations of state and phase boundary for stishovite and $CaCl_2$-type $SiO_2$. *Am. Mineral.* **103**, 792–802 (2018).
50. S. Brygoo, M. Millot, P. Loubeyre, A. Lazicki, S. Hamel, T. Qi, P. Celliers, F. Coppari, J. Eggert, D. Fratanduono, D. Hicks, J. Rygg, R. Smith, D. Swift, G. Collins, R. Jeanloz, Analysis of laser shock experiments on precompressed samples using a quartz reference and application to warm dense hydrogen and helium. *J. Appl. Phys.* **118**, 195901 (2015).
51. S.-N. Luo, O. Tschauner, P. D. Asimow, T. J. Ahrens, *A new dense silica polymorph: A possible link between tetrahedrally and octahedrally coordinated silica*, *Am. Min.* **89**, 455–461 (2004).
52. T. Sekine, M. Akaishi, N. Setaka, $Fe_2N$-type $SiO_2$ from shocked quartz. *Geochim. Cosmochim. Acta* **51**, 379–381 (1987).
53. M. A. Meyers, *Dynamic Behavior of Materials* (John Wiley & Sons, Inc, New York, 1994).
54. F. Wang, Y. Tange, T. Irifune, K. I. Funakoshi, P-V-T equation of state of stishovite up to mid-lower mantle conditions. *J. Geophys. Res. Solid Earth* **117**, B06209 (2012).


**Acknowledgments:** High-pressure synthesis experiments were conducted at the B1 station of the Synergetic Extreme Condition User Facility (SECUF), Jilin University. The XRD experiments were performed at BL3 of SACLA with the approval of the Japanese Synchrotron Radiation Research Institute (proposal nos. 2021A8642 and 2021A8017). The experiments were conducted under the joint research of ILE. The calculations were carried out using supercomputers at the High-Performance Computing Center of Collaborative Innovation Center of Advanced Microstructures, the high-performance supercomputing center of Nanjing University. **Funding:** This work was supported by the National Nature Science Foundation of China grants 11804010, U2230401, 11904119, 11974131, and 41974099 (W.Y.); Shanghai Key Laboratory of Material Frontiers Research in Extreme Environments grant 22dz2260800 (T.Se.); Shanghai Science and Technology Committee grant 22JC1410300 (T.Se.); National Natural Science Foundation of China grants 12125404 and T2495231 (J.S.); Basic Research Program of Jiangsu grant BK20233001 (J.S.); AI & AI for Science program of Nanjing University, and the Fundamental Research Funds for the Central Universities. (J.S.); National Natural Science Foundation of China grant 123B2049 (S.P.); JSPS KAKENHI grant 20H00139 (N.O.); JSPS KAKENHI grants 22K18702 and 23K20038 (N.O.); JSPS Core-to-Core program grant JPJSCCA20230003 (N.O.); and MEXT Q-LEAP grant JP-MXS0118067246 (N.O.). **Author contributions:** Conceptualization: W.Y. and T.Se. Methodology: X.F., S.P., K.K., and J. Shi Visualization: X.F. and S.P. Investigation: X.F., S.P., K.K., J. Shi, W.Y., and T.Se. Supervision: W.Y., T.Se., and J.S. Writing–original draft: X.F., S.P., and K.K. Writing–review and editing: All authors. **Competing interests:** The authors declare that they have no competing interests. **Data and materials availability:** All data needed to evaluate the conclusions in the paper are present in the paper and/or the Supplementary Materials, and on Open Archive Zenodo (https://doi.org/10.5281/zenodo.14253000).

Submitted 11 August 2024
Accepted 20 March 2025
Published 25 April 2025
10.1126/sciadv.ads3139